ACS APPLIED MATERIALS & INTERFACES

Forum Article

www.acsami.org

Comparison of the Properties of Cellulose Nanocrystals and Cellulose Nanofibrils Isolated from Bacteria, Tunicate, and Wood Processed Using Acid, Enzymatic, Mechanical, and Oxidative Methods

Iulia A. Sacui,[†,‡] Ryan C. Nieuwendaal,[†] Daniel J. Burnett,[§] Stephan J. Stranick,[⊥] Mehdi Jorfi,[#] Christoph Weder,[#] E. Johan Foster,[#] Richard T. Olsson,[∥] and Jeffery W. Gilman*[,†]

[†]Materials Science and Engineering Division and [⊥]Materials Measurement Science Division, National Institute of Standards and Technology, Gaithersburg, Maryland 20899, United States

[‡]Department of Physics, Georgetown University, Washington, DC, 20057, United States

[§]Surface Measurement Systems LTD., N.A., Allentown, Pennsylvania 18103, United States

[#]Adolphe Merkle Institute, University of Fribourg, Rte de l'Ancienne Papeterie, CH-1723 Marly, Switzerland

[∥]Department of Fibre and Polymer Technology (WWSC), School of Chemical Science and Engineering, Royal Institute of Technology, 100 44 Stockholm, Sweden

Supporting Information

ABSTRACT: This work describes the measurement and comparison of several important properties of native cellulose nanocrystals (CNCs) and cellulose nanofibrils (CNFs), such as crystallinity, morphology, aspect ratio, and surface chemistry. Measurement of the fundamental properties of seven different CNCs/CNFs, from raw material sources (bacterial, tunicate, and wood) using typical hydrolysis conditions (acid, enzymatic, mechanical, and 2,2,6,6-tetramethylpiperidinyl-1-oxyl (TEMPO)-mediated oxidation), was accomplished using a variety of measurement methods. Atomic force microscopy (AFM), transmission electron microscopy (TEM), and ^{13}C cross-polarization magic angle spinning (CPMAS) nuclear magnetic resonance (NMR) spectroscopy were used to conclude that CNCs, which are rodlike in appearance, have a higher crystallinity than CNFs, which are fibrillar in appearance. CNC aspect ratio distributions were measured and ranged from 148 ± 147 for tunicate-CNCs to 23 ± 12 for wood-CNCs. Hydrophobic interactions, measured using inverse gas chromatography (IGC), were found to be an important contribution to the total surface energy of both types of cellulose. In all cases, a trace amount of naturally occurring fluorescent compounds was observed after hydrolysis. Confocal and Raman microscopy were used to confirm that the fluorescent species were unique for each cellulose source, and demonstrated that such methods can be useful for monitoring purity during CNC/CNF processing. This study reveals the broad, tunable, multidimensional material space in which CNCs and CNFs exist.

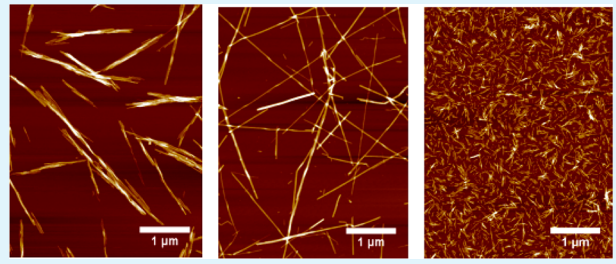

KEYWORDS: *nanocellulose, AFM, TEM, NMR, IGC, Raman, fluorescence*

INTRODUCTION

Cellulose is the most abundant organic polymer on Earth and can be found in plants (e.g., cotton,[1] hemp,[2] wood[3]), marine animals (e.g., tunicates[4]), algae (e.g., *Valonia*[5]), bacteria (e.g., *Acetobacter xylium*[6]), and even amoeba (*Dictyostelium discoideum*[7]). The isolation of cellulose nanocrystals (CNCs) from ramie and cotton fibers by sulfuric acid treatment goes back to the work by Mukherjee and Woods in 1953.[1] Acid hydrolysis of the native cellulose is the predominant method used to isolate CNCs and cellulose nanofibrils (CNFs), which we collectively refer to as nanocellulose. To meet the emerging commercial demand, several pilot plants and a number of commercial-scale CNC and CNF manufacturing facilities have recently been established around the world utilizing wood as the raw material.[8,9] Depending on the source of the nanocellulose and the chemical treatment, the resulting material can vary in crystal structure, degree of crystallinity, surface chemistry, morphology and aspect ratio.[10] The abundant and easily modified hydroxyl surface functionality of nanocellulose provides for ease in introducing ionic groups (sulfate,[11] carboxylate[12]), catalytic groups (ammonium[13]), and polymerizable groups.[14] However, complete control over the various material parameters has yet to be realized.

Although a wealth of information is available on methods to isolate the CNCs/CNFs and on methods for introducing a

Special Issue: Applications of Hierarchical Polymer Materials from Nano to Macro

Received: January 17, 2014
Accepted: March 18, 2014
Published: April 18, 2014

   dx.doi.org/10.1021/am500359f | *ACS Appl. Mater. Interfaces* 2014, 6, 6127−6138

variety of functional groups, simultaneous control over the parameters such as aspect ratio and modulus[15] has not yet been achieved. This has not deterred researchers in applying nanocellulose in a wide variety of applications because of their intriguing properties such as low thermal expansion, optical transparency,[16] renewability, biodegradability, low cost and low toxicity.[17] Besides their use as a reinforcing filler for polymers,[18] CNCs and CNFs have been utilized to fabricate a wide range of other functional materials, including photonic crystals,[19] barrier films,[20] shape-memory polymers,[21] light-healable,[22] drug-delivery,[23] and mechanically adaptive nanocomposites,[24−26] and they enable applications that range from membranes for water-treatment[27] to biomedical devices.[18,10,28]

Critical features for structural applications of nanocellulose include dimensions[29] (because this determines surface area and aspect ratio), strength/toughness, modulus,[30] and surface functionality. All of these parameters help to provide unique nanoscale reinforcement mechanisms. For example, surface functionality is important because this determines the manner in which nanocellulose interacts with itself (nanofiber−nanofiber interactions) and with polymers[31] via ionic, hydrogen-bonding, and hydrophobic interactions.[32] Aspect ratio, as well as surface area, and functionality, are also critical material parameters since they affect the rheological properties, which in turn control processing and manufacturing ability. The crystallinity of nanocellulose is critical because it is directly related to modulus, and increased modulus is often desirable in lightweight composite applications.

Impurities in the nanocellulose samples can lower thermal stability, which is a concern in flame retardant and high-temperature applications.[33] Impurities that introduce defects can lower performance in thin-film barrier applications, reduce toughness in structural applications, and can absorb or scatter light, degrading their performance in optical applications. Impurities with different chemical composition than the nanocellulose can also cause device rejection in biomedical implants.[34]

Previously, a wide variety of measurements have been employed to characterize various aspects and properties of nanocelluloses, though in most cases the techniques being employed only focused on two or three types of nanocelluloses, or if comparing several nanocelluloses, relied on a limited number of characterization methods (see Table S1 in the Supporting Information). Techniques such as scanning probe microscopy, helium ion microscopy, near-infrared-Raman spectroscopy, Raman microscopy, solid-state nuclear magnetic resonance (NMR) spectroscopy, Förster resonance energy transfer (FRET), and other fluorescence imaging methods have recently been used to expand our understanding of nanocellulose structure and properties.[34,35] With the growing importance of nanocellulose, the development of new characterization tools and data are needed to enable elucidation of their structure−property relations and for successful manufacturing and product development of cellulose nanomaterials.[36,37,34]

Measurement of the fundamental properties of CNCs and CNFs is a prerequisite for the development of critical structure−property and structure−processing relationships across a broad range of applications. In this paper, we report on the characterization of CNCs and CNFs isolated from various raw material sources (bacterial, tunicate, and wood) using typical hydrolysis conditions (acid, enzymatic, mechanical, and 2,2,6,6-tetramethylpiperidinyl-1-oxyl (TEMPO)-mediated oxidation). Characterization methods include atomic force microscopy (AFM), transmission electron microscopy (TEM), ^{13}C cross-polarization magic angle spinning (CPMAS) nuclear magnetic resonance (NMR) spectroscopy, inverse gas chromatography (IGC), and Raman and fluorescence microscopy. This comprehensive approach to the characterization was taken to provide a detailed set of information on representative nanocellulose samples where the measurements were all made under identical sample preparation conditions, using the same instruments, and the same data interpretation software or algorithms, and thereby provide a useful resource for those working to study and apply nanocellulose (see data summary in Table S2 in the Supporting Information).

EXPERIMENTAL SECTION

Certain commercial equipment, instruments, materials or companies are identified in this paper in order to adequately specify the experimental procedure. Such identification is not intended to imply recommendation or endorsement by the National Institute of Standards and Technology, nor is it intended to imply that the materials or equipment identified are necessarily the best available for this purpose. This work was carried out by the National Institute of Standards and Technology (NIST), an agency of the U.S. government, and by statute is not subject to copyright in the United States.

Bacterial Cellulose-Acid Hydrolysis. Bacterial cellulose was grown from a sterilized glucose medium inoculated with *Acetobacter xylinum* − ATCC 23767, according to established protocols.[38] The extracted bacterial cellulose was hydrolyzed using sulfuric or hydrochloric acid (37% by mass) for 48 h at 60 °C. The resulting suspensions were then washed with water and isothermally centrifuged.

Tunicate Cellulose-Sulfuric Acid Hydrolysis. CNCs were isolated from tunicates (*Styela clava*) collected from floating docks in Point View Marina (Narragansett, RI). The CNCs were prepared by sulfuric acid hydrolysis (48% by mass) of the cellulose pulp, according to established protocols,[39] with slight modifications, as previously reported.[40]

Wood Cellulose-Enzymatic Hydrolysis. Commercial wood pulp with hemicellulose and lignin contents of 13.8% and 0.7% (from Nordic Paper, Sweden), was used as raw material for the extraction. The extraction was carried out post an initial aqueous enzymatic (endoglucanase Novozyme 476) pretreatment at 50 °C for 2 h (0.1 mL of enzyme was used per 40 g of dry cellulose material suspended in 2 L). The enzyme treatment was followed by 8 passes through a M-110EH microfluidizer at maximum pressure 1100 bar (Microfluidcs Ind., USA). The resulting suspensions were then washed with water and isothermally centrifuged.

Wood Pulp-Mechanically Refined. Mechanically refined wood CNFs were purchased from The Process Development Center at The University of Maine. Briefly, southern bleached softwood pulp was refined in a multistage disk refiner.

Wood Pulp-Sulfuric Acid Hydrolysis. Wood CNCs were purchased from The Process Development Center at The University of Maine and manufactured at the U.S. Forest Products Laboratory. Briefly, wood pulp was hydrolyzed using sulphuric acid (64% by mass).

Wood Cellulose-TEMPO Mediated Oxidation. Commercial wood pulp with hemicellulose and lignin contents of 13.8% and 0.7% (from Nordic Paper, Sweden), was used as raw material for the extraction. Wood pulp (40 g) was suspended in water (4 L), containing 0.64 g of oxidation mediator 2,2,6,6-tetramethylpiperidinyl-1-oxyl (TEMPO) and 4 g of sodium bromide. The oxidation was carried out by adding 2 mol/L NaClO (10 mmol per gram of cellulose) to the suspension. The pH of the suspension was maintained at 10 by adding 0.5 mol/L NaOH with a pH stat for 5 h. The reaction was then quenched by adding ethanol (ca. 0.2 L). The resulting suspensions were then washed with water and isothermally centrifuged.

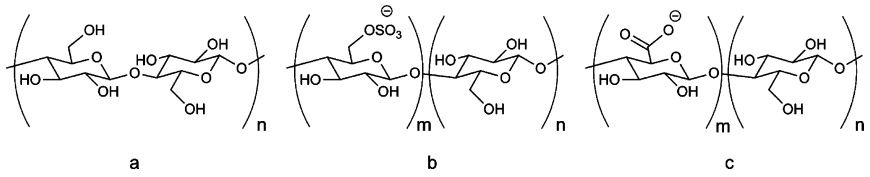

Figure 1. Chemical structure of nanocellulose surface: (a) mechanically refined, enzymatic hydrolyzed, and HCl hydrolyzed; (b) sulfuric acid hydrolyzed; and (c) TEMPO-modified.

^{13}C Cross-Polarization Magic Angle Spinning (CPMAS) Nuclear Magnetic Resonance (NMR). Solid-state NMR experiments were performed at 100 MHz (2.35 T) on a Tecmag Apollo spectrometer, ultrawide bore Nalorac magnet, and in-house designed 7.5 mm double resonance magic angle spinning probe. Each sample (≈100 mg freeze-dried nanocellulose) was pressed into a 6 mm × 7 mm disk, placed into a Macor rotor, and spun at 3800 ± 100 Hz. CPMAS NMR experiments were performed with the following conditions: 25.19 MHz ^{13}C frequency, 100.16 MHz ^{1}H frequency, 3.2 μs ^{1}H $\pi/2$ pulse, 2 ms contact time, 72 kHz ^{13}C contact pulse, 68 kHz ^{1}H contact pulse, 78 kHz continuous wave (cw) decoupling, 100 μs dwell time, 600 data points with 15784 zero filling points, 2048 to 8196 scans, 3 s recycle delay, and 8192 to 32768 transients. The ^{1}H cw decoupling frequency was set to 1.3 ppm relative to tetramethylsilane (TMS) at 0 ppm. The frequency scale of the ^{13}C NMR spectra were referenced to TMS (0 ppm) utilizing adamantane as a secondary reference.

Transmission Electron Microscopy (TEM). High-contrast transmission electron microscopy (TEM, Hitachi HT-7700, Japan) was used to determine the morphology of the nanocellulose deposited from the as-prepared suspensions. Ca. 0.02% by mass aqueous suspensions of the nanocellulose samples were sonicated for 5 s before deposition onto TEM grids (ultrathin carbon film/holey carbon 400 mesh, Ted Pella, USA) and dried overnight at room temperature. No staining was used. The TEM was operated at 80 kV acceleration voltage 24 h after the sample preparation.

Atomic Force Microscopy (AFM). AFM measurements were carried out using a Dimension Icon (Bruker, Billerica, MA). Substrates were prepared by drop casting poly-L-lysine (PLL) solution (0.01% by mass) onto a freshly cleaved mica substrate.[36] After 5 min, the substrate was blown dry. Diluted aqueous nanocellulose suspensions (ca. 0.02% by mass) were deposited onto the PLL-coated mica disks. The samples were rinsed with water after 5 min to remove unattached nanocellulose and then blown dry. Topographical imaging was performed in Scanasyst tapping mode using a Scanasyst-air tip (Bruker, Billerica, MA), with nominal radius of 2 nm.

Inverse Gas Chromatography (IGC). Surface energy analyses were carried out using an IGC surface energy analyzer (SEA) (Surface Measurement Systems, Alperton, UK) and the data were analyzed using both standard and advanced SEA Analysis Software. IGC surface energy measurements and analysis calculations were conducted at finite dilutions according to the published procedure.[41−45] Briefly, approximately 45 mg of freeze-dried CNC was packed into individual silanized glass columns. Each column was conditioned, dried under a flow of anhydrous helium for 2 h, before n-alkane probe molecules (decane, nonane, octane, and heptane) and polar probe molecules (acetone, ethanol, acetonitrile, ethyl acetate, and dichloromethane) were introduced over a range of injection volumes. This method was used to determine the dispersive and acid−base components of surface energy as a function of fractional surface coverage. This method also permits the investigation of energetic heterogeneity.

Confocal Microscopy. Dilute nanocellulose suspensions were deposited onto an ultraviolet ozone (UVO)-treated glass coverslips and dried overnight at room temperature. Confocal microscopy measurements were carried out using an upright Leica TCS SP5 II (Leica Microsystems, Buffalo Grove, IL), with a 10×, 0.30 numerical aperture (NA) air objective. Images were acquired by exciting at 488 nm and collecting emission at 500 to 550 nm.

Confocal Raman Microscopy (CRM). Dilute CNC suspension was deposited onto an ultraviolet ozone (UVO)-treated glass coverslip and dried overnight at room temperature. Raman spectra were collected on an in-house designed confocal Raman system which was based on a setup described in detail elsewhere.[46] Briefly, the samples were illuminated by 488 nm laser radiation passed through an "inject-reject" notch-filter and focused on the sample using a 60× oil-immersion lens of numerical aperture 1.49. Scattered Raman light was collected by the lens, passed back through the notch-filter, and analyzed with a high resolution spectrograph. Single-mode optical fibers coupled the laser and spectrograph to the system to provide an input Gaussian beam and confocal imaging of the output scattered light. The excitation power was set to 2 mW at the sample. This power level provided sufficient reduction of the sample's intrinsic autofluorescence through photobleaching during the initial phase of the experiment and provided high fidelity Raman measurements.

RESULTS AND DISCUSSION

Naturally occurring cellulose is a hierarchically structured material, which at the lowest hierarchical level (the cellulose polymer chain−chain interaction level) contains both highly crystalline, as well as amorphous domains.[10] These amorphous regions can undergo hydrolysis to yield cellulose nanocrystals and nanofibrils with a range of crystallinities, moduli, surface chemistries, surface energies, and aspect ratios. Sulfuric acid hydrolysis is the most common hydrolysis technique, because it creates CNCs that are dispersible in water due to a small number of sulfate ester groups introduced to the surface of the CNCs during hydrolysis.[11,47] Similarly, TEMPO-mediated oxidation modifies the CNC surface with the oxidation of primary hydroxyls to carboxylate groups.[12] On the other hand, enzymatic, mechanical refining, and HCl hydrolysis leave the surface chemistry of the CNC unchanged.[10] The chemical surface structures present on the various CNCs are shown in Figure 1. In this article, we focus on nanocellulose isolated from wood, bacteria, and tunicates. The cellulose source, hydrolysis technique, and abbreviation for each sample are given in Table 1.

Table 1. Cellulose Sources and Hydrolysis Techniques Used to Produce the Nanocellulose Samples Used in This Study

source	hydrolysis technique	surface chemistry	abbreviation
bacterial cellulose	hydrochloric acid	hydroxyl (neutral)	bacterial-HCl
bacterial cellulose	sulfuric acid	sulfate (negative)	bacterial-sulfate
tunicate cellulose	sulfuric acid	sulfate (negative)	tunicate-sulfate
wood pulp	enzymatic	hydroxyl (neutral)	wood-enzymatic
wood pulp	mechanically refined	hydroxyl (neutral)	wood-mechanically refined
wood pulp	sulfuric acid	sulfate (negative)	wood-sulfate
wood pulp	TEMPO-mediated oxidation	carboxylate (negative)	wood-TEMPO

Crystallinity. ^{13}C cross-polarization magic angle spinning (CPMAS) nuclear magnetic resonance (NMR) spectroscopy is a powerful tool for quantifying the crystalline content in cellulose fibers, in particular crystalline fraction and polymorph (i.e., cellulose I-α, I-β, II).[48] Wide-angle X-ray scattering (WAXS), a more commonly used method for measuring crystalline fraction of nanocelluloses,[49] provides a measurement for the total volume fraction of crystalline cellulose, whereas CPMAS NMR counts only cellulose chains that are present within the interior of the CNC. Cellulose chains on the crystal surface are counted in the disordered fraction, so crystallinity values calculated from NMR are, by comparison to WAXS, smaller.[49] Our approximated crystallinity values are, as a result, lower bound on the total crystalline fraction.

For the quantification of crystalline content in the seven materials prepared here, we performed ^{13}C CPMAS and $T_{1\rho}{}^{H}$-filtered CPMAS NMR experiments. The $T_{1\rho}{}^{H}$ relaxation times of crystalline cellulose domains are longer than the noncrystalline domains, so spectral editing by way of $T_{1\rho}{}^{H}$ offers an avenue for discriminating between crystalline vs noncrystalline domains. In Figure 2a, we have displayed the CPMAS spectrum of bacterial cellulose-HCl, including the assignments of the carbons on the six-membered ring of the monomer unit.

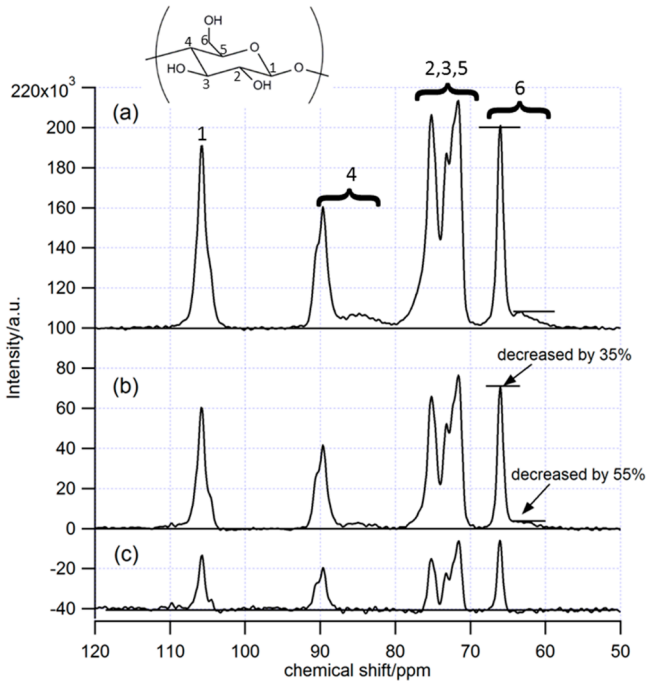

Figure 2. ^{13}C NMR spectra of bacterial-HCl cellulose: (a) CPMAS spectrum, (b) $T_{1\rho}{}^{H}$-filtered CPMAS spectrum, and (c) the difference spectrum (spectrum b − 0.55·spectrum a).

As shown in Figure 2a, carbons 4 and 6 (henceforth denoted C4 and C6) both exhibit two resonances with the same general pattern; an intense resonance and a weaker resonance at approximately 5 ppm upfield. Following the assignments determined previously,[50,51] these features are due to the crystalline and noncrystalline components of cellulose, respectively. When introducing a 7 ms $T_{1\rho}{}^{H}$ relaxation filter, we observe that the resonances associated with the crystalline and noncrystalline regions decay at different rates. We have displayed horizontal lines in panels a and b in Figure 2 as a guide to the eye. As shown in Figure 2b, after a 7 ms ^{1}H spin lock pulse, the noncrystalline resonances (62 ppm and 85 ppm) have decayed 55% in intensity, whereas the crystalline components have decreased in intensity only 35%. This difference in decay rates allows us to separate the spectra of the two components (noncrystalline vs crystalline) as shown in Figure 2c. When taking the difference (spectrum 2b − 0.55· spectrum 2a), one is able to isolate the spectrum of the crystalline phase, which is represented in Figure 2c. By comparison to previously published ^{13}C NMR spectra of cellulose,[50,51] we assign this spectrum to form I-α.

Similar experiments were performed on the remaining nanocellulose samples. The corresponding ^{13}C CPMAS spectra are shown in Figure 3 and the crystalline fractions are given in

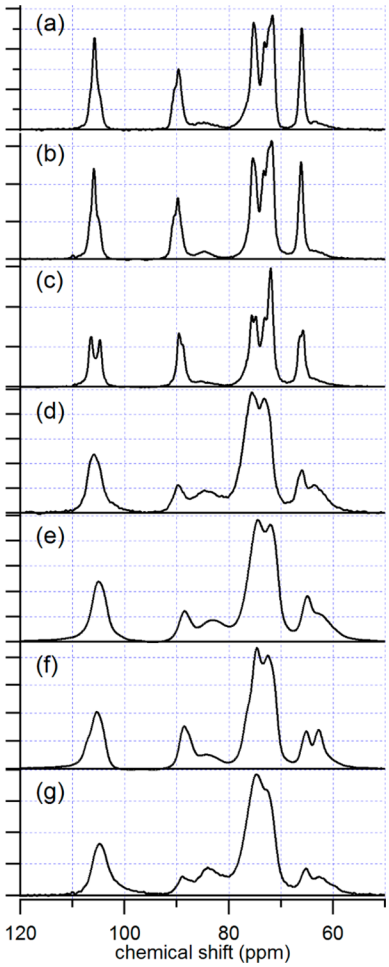

Figure 3. ^{13}C CPMAS spectra of (a) bacterial-HCl, (b) bacterial-sulfate, (c) tunicate-sulfate, (d) wood-enzymatic, (e) wood-mechanically refined, (f) wood-sulfate, and (g) wood-TEMPO nanocelluloses.

Table 2, noting that cellulose chains on the crystal surfaces contribute to noncrystalline intensity in the NMR measurement, and not crystalline intensity. We also include the assignments of the crystalline forms observed from the ^{13}C CPMAS spectra for all of the samples in Table 2.

As shown in Table 2, both bacterial nanocellulose types (HCl and sulfate) exhibit the same polymorph (form I-α) as well as nominally the same total crystalline content (0.72). The tunicate cellulose, while also highly crystalline (0.80), exhibits the polymorph form I-β. All of the wood cellulose samples have much lower crystallinity (0.60 to 0.05). Some of the wood

dx.doi.org/10.1021/am500359f | ACS Appl. Mater. Interfaces 2014, 6, 6127−6138

Table 2. Crystalline Fractions and Polymorph Assignments of the Nanocellulose Samples, as Measured by CPMAS NMR[a]

cellulose source	crystalline fraction	predominant polymorph/ form
bacterial-HCl	0.74	I-α
bacterial-sulfate	0.72	I-α
tunicate-sulfate	0.80	I-β
wood-enzymatic	0.30	I-α (disordered)
wood-mechanically refined	0.55	I-α
wood-sulfate	0.60	I-α (disordered)
wood-TEMPO	0.05	unknown

[a]Estimated error for the crystalline fraction is ±0.03. The error estimate is based on uncertainty in the spectrum of the noncrystalline phase as well as signal-to-noise limitations.

samples exhibit a crystalline phase spectrum that is consistent with form I-α, but with resonances that are seemingly much broader than the other more highly crystalline bacterial celluloses. We speculate that the molecular packing in the wood samples are likely similar to the form I-α, albeit more disordered with less uniform packing environments.

Structural Morphology. Transmission electron microscopy (TEM) and atomic force microscopy (AFM) images were taken to examine structural differences between the nanocellulose samples. As seen from Figures 4 and 5, both size and aspect ratio depend strongly on the cellulose source and the hydrolysis technique, and each source/process combination yields a CNCs or CNFs with distinct characteristics. Acid hydrolysis techniques, both hydrochloric acid and sulfuric acid, yield rodlike nanocrystals with high crystalline fractions (0.60 to 0.80) (Figures 4 and 5 (a, b, c, and f)). The source of the cellulose is also a major factor in the morphology and size of the nanocrystals. For instance, bacterial-sulfate, tunicate-sulfate and wood-sulfate CNCs show pronounced differences (Figures 4 and 5 (b, c, and f)). The bacterial CNCs appear to be bundled or aggregated,[38] whereas the tunicate CNCs appear to be much more individualized. The bundling of the bacterial nanocellulose can be due to electrostatic attraction of the nanofibers, or the remnants of a small amount of paracystalline cellulose holding the rods together.[52] Close packing or bundling was also seen with the wood-sulfate CNCs.

To examine the effect of the processing technique on nanocellulose morphology, while keeping the cellulose source constant, wood pulp was treated with four different processing methods: enzyme hydrolysis, mechanical refiner, sulfuric acid, and TEMPO-mediated oxidation. Enzyme hydrolysis of wood pulp leads to a network of nanofibrils (Figures 4d and 5d).[53] Mechanically refining the wood pulp with no added chemicals yields the largest nanofibers of all the cellulose samples (Figures 4e and 5e). Sulfuric acid hydrolysis of wood pulp produces short rod-like CNCs that appear to be bundled (Figures 4f and 5f). TEMPO-mediated oxidation of wood pulp yields extremely thin nanofibers with the lowest crystalline fraction (0.05) (Figure 4g and 5g). Indeed, the range of morphologies and crystallinities observed for nanocellulose isolated from wood, by simply varying the processing, reveals the tunability of CNCs. There is correlation between the crystalline fraction and the apparent rigidity of the nanocellulose. Networked and ribbon-like wood CNF samples had a lower crystalline fraction (0.05 to 0.55) compared to rodlike wood-sulfate (0.60). It is also true that some of the variation in morphology and crystallinity could be from the different wood sources used here.

Aspect Ratio. Aggregation, bundling, formation of nanofibrilar networks, and overlapping of individual CNCs and CNFs make accurate dimension measurements difficult, even using current image analysis techniques. For this reason, only well-dispersed nanocellulose samples, where both ends of the individual fiber could be clearly identified, were measured. The negatively charged sulfated CNCs were the best dispersed samples; therefore, size and aspect ratio distributions were measured for bacterial-sulfate, wood-sulfate, and tunicate-sulfate CNCs.

Size and aspect ratio measurements of individual CNCs were based on the evaluation of AFM images (Figure 6). The apparent width of the CNCs is larger than the actual value because of AFM tip convolution;[54] therefore, the aspect ratio was calculated as the length L divided by the height h for each

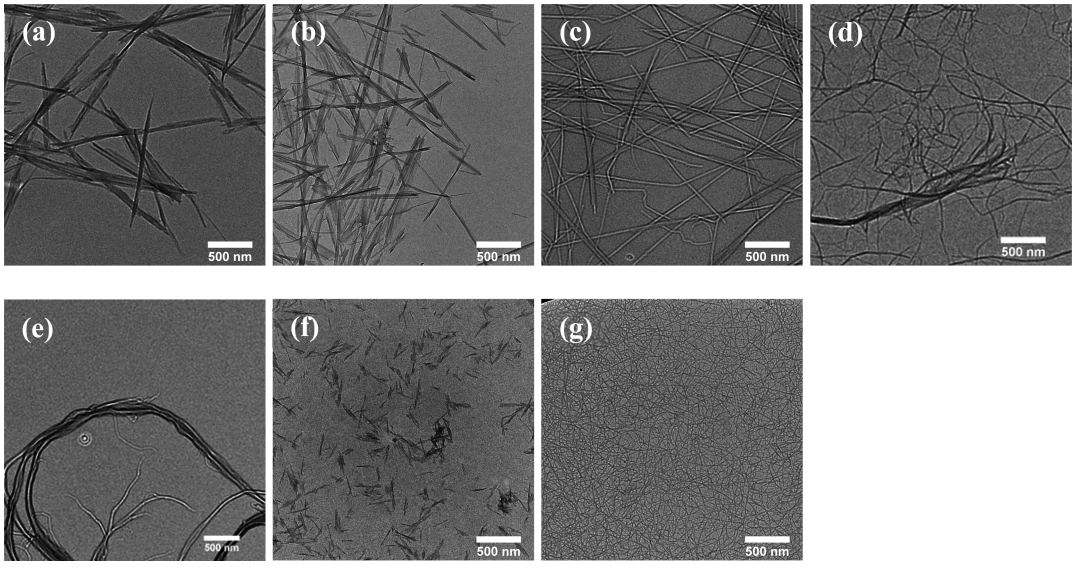

Figure 4. TEM images of (a) bacterial-HCl, (b) bacterial-sulfate, (c) tunicate-sulfate, (d) wood-enzymatic, (e) wood-mechanically refined, (f) wood-sulfate, and (g) wood-TEMPO.

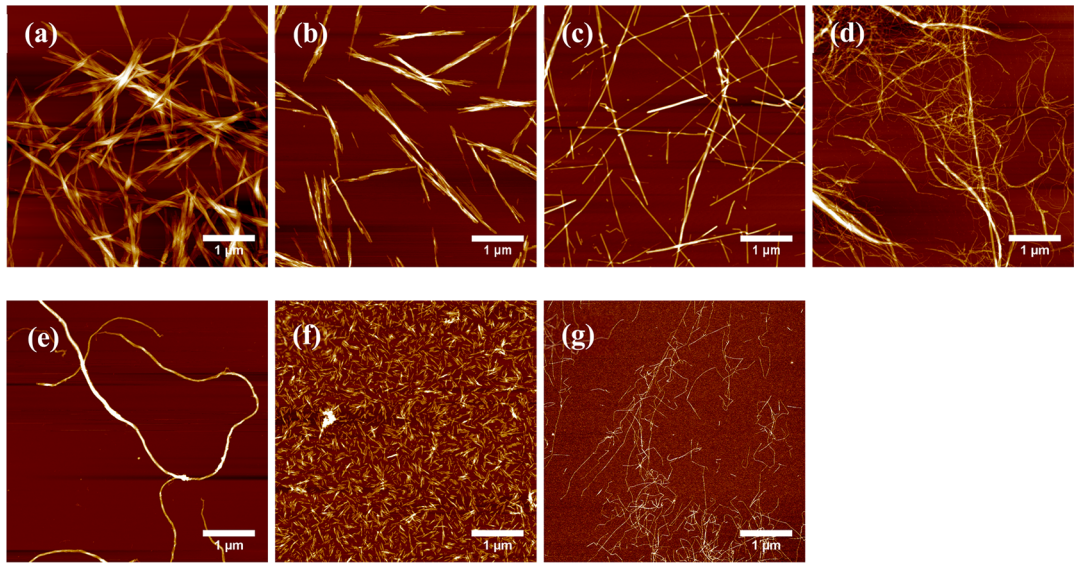

Figure 5. AFM topography images showing height measurements of (a) bacterial-HCl, (b) bacterial-sulfate, (c) tunicate-sulfate, (d) wood-enzymatic, (e) wood-mechanically refined, (f) wood-sulfate, and (g) wood-TEMPO.

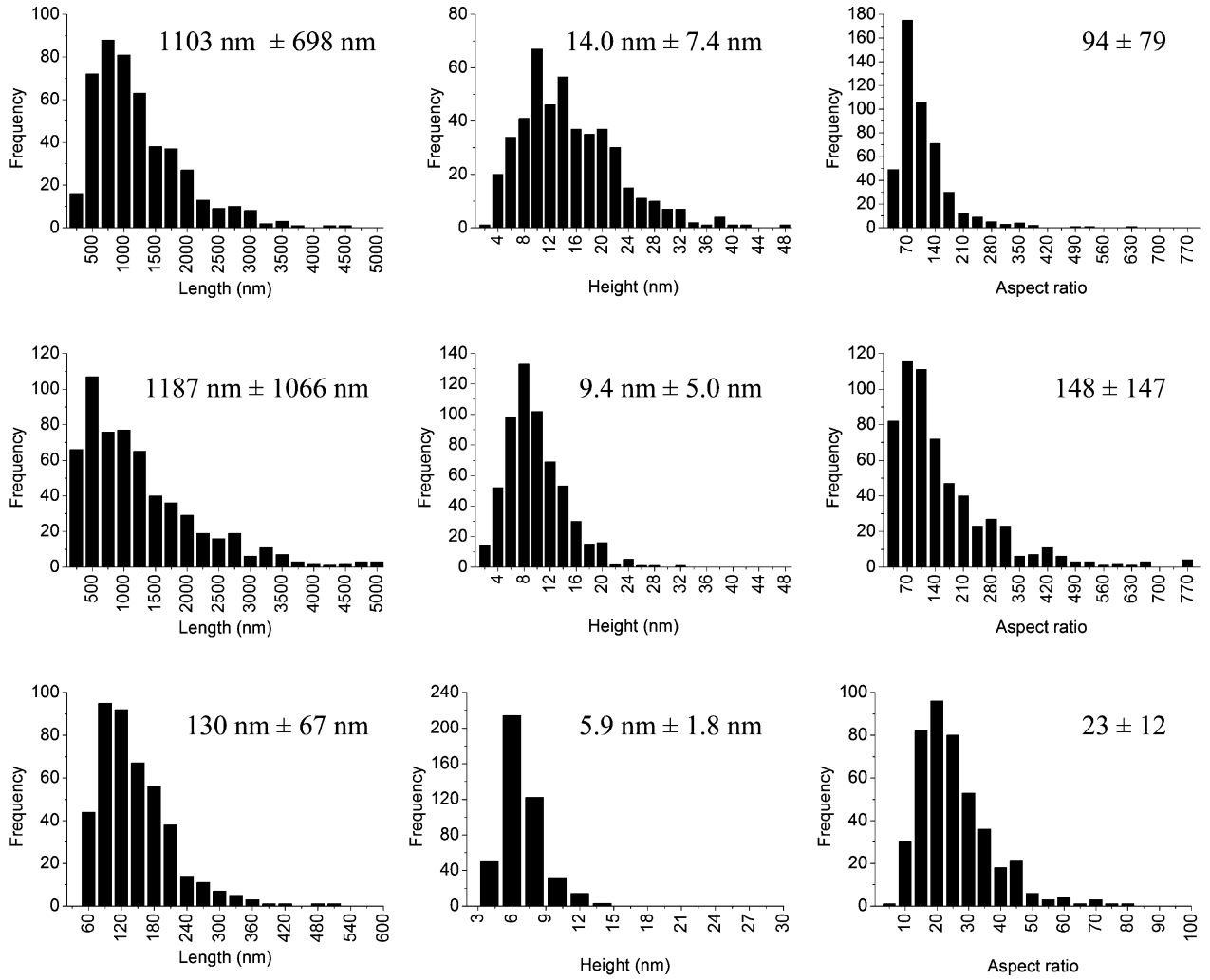

Figure 6. Length (left column), height (middle column), and aspect ratio (right column) distribution histograms and average values ± one standard deviation for bacterial-sulfate (top row), tunicate-sulfate (middle row), and wood-sulfate (bottom row).

individual CNC, because these dimensions are not significantly affected by tip convolution. More detailed information on the length, height, and aspect ratio measurements can be found in the Supporting Information. Aspect ratio measurements can

dx.doi.org/10.1021/am500359f | ACS Appl. Mater. Interfaces 2014, 6, 6127−6138

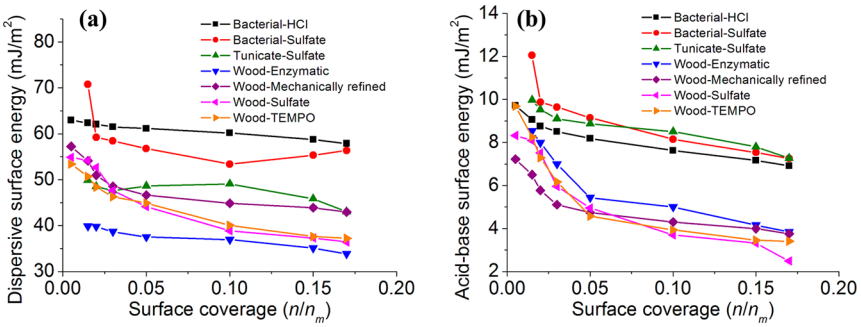

Figure 7. (a) Dispersive and (b) acid–base surface energy profiles for the nanocellulose samples measured at 30 °C. Fraction surface coverage is the number of moles (n) divided by the moles required to cover a surface monolayer (n_m).

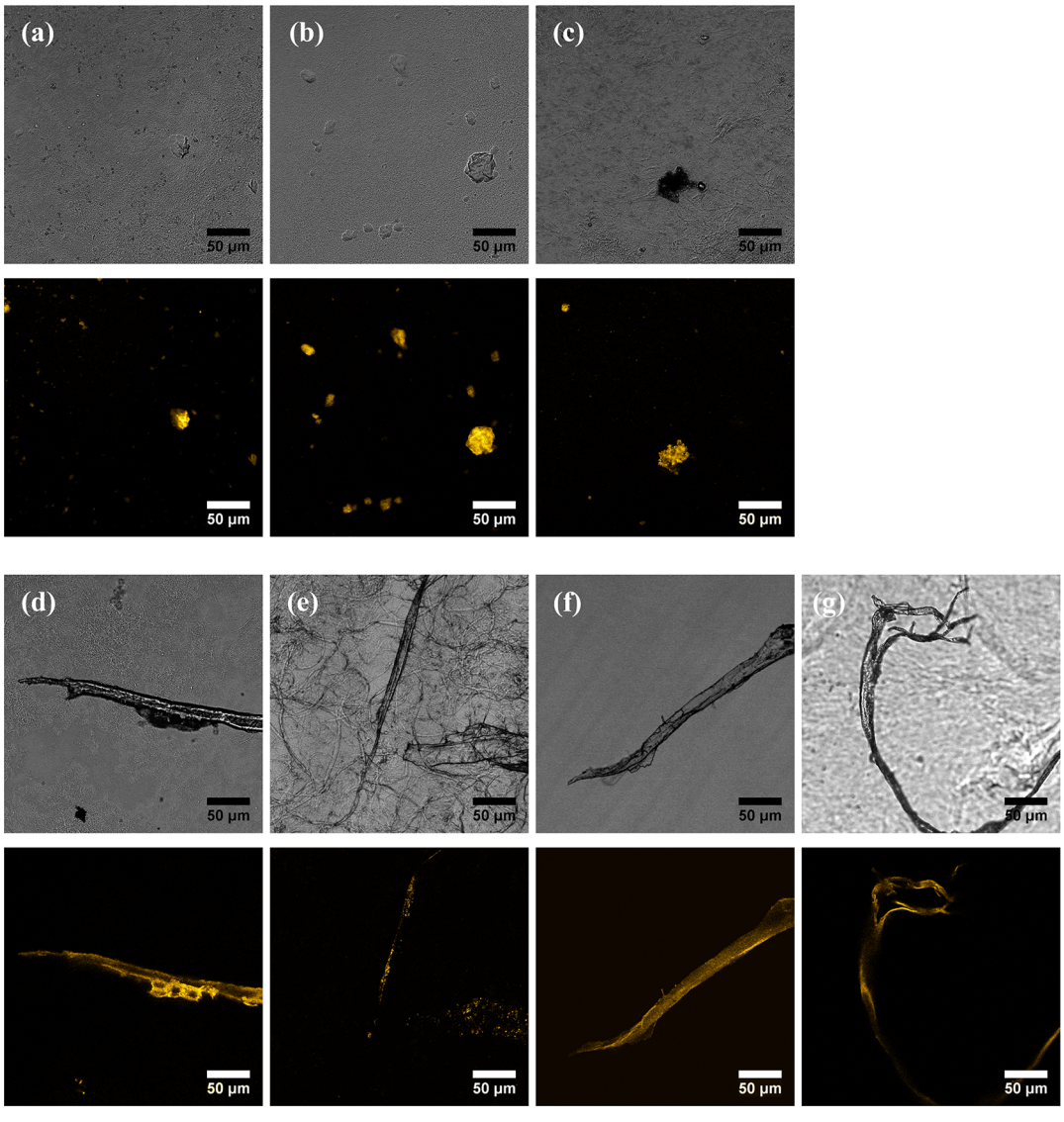

Figure 8. Intensity-based LSCM images of nanocellulose showing reflection images (top row) and their corresponding autofluorescent areas (bottom row) for (a) bacterial-HCl, (b) bacterial-sulfate, (c) tunicate-sulfate, (d) wood-enzymatic, (e) wood-mechanically refined, (f) wood-sulfate, and (g) wood-TEMPO.

also be taken from TEM images, but limited image contrast and damage from the electron beam motivated our use of AFM imaging.[55] Also, AFM is becoming more widely accessible, and therefore this technique may be a better routine tool than TEM.

Previous work shows that the size of the CNCs is strongly dependent on the hydrolysis conditions.[56] Typically, stronger acid conditions, longer reaction times and higher temperatures tend to yield shorter CNCs. There is a correlation between the crystalline fraction and the aspect ratio for the sulfated CNCs. The high crystalline fraction (0.80) of the tunicate-sulfate

dx.doi.org/10.1021/am500359f | ACS Appl. Mater. Interfaces 2014, 6, 6127–6138

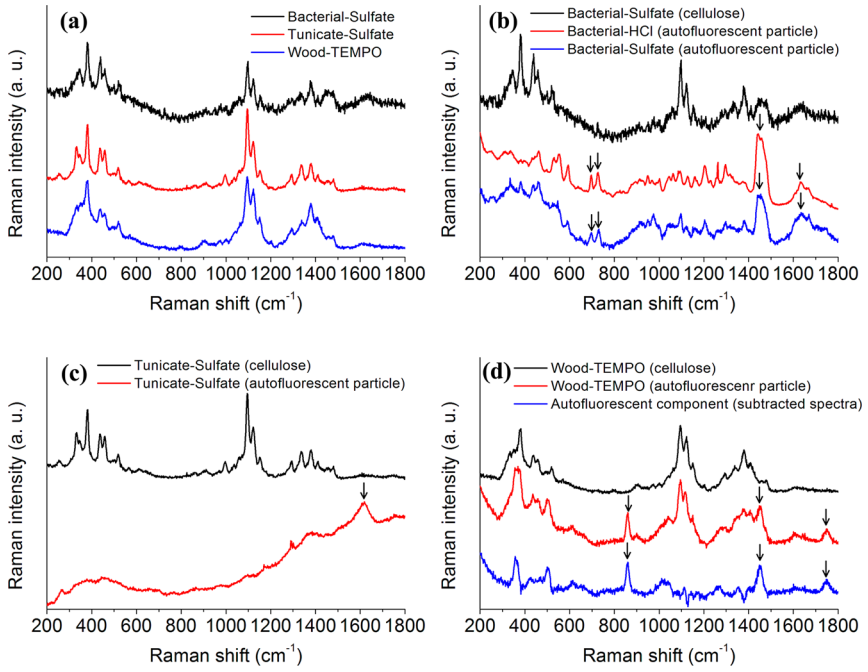

Figure 9. Raman spectra of nanocellulose samples. (a) Graph showing Raman spectra of cellulose portion for three samples and (b–d) graphs highlighting the differences in Raman spectra between the cellulose portion and the autofluorescent hydrolysis resistant particles present in the samples.

CNCs lead to longer rodlike particles with a higher aspect ratio (148), whereas the lower crystalline fraction (0.60) of the wood-sulfate CNCs yielded shorter rodlike particles with a lower aspect ratio (23) (Figure 6).

In the case of bacterial-sulfate, the longer fibers were also thicker, keeping their aspect ratio low. The average length reported in the literature for bacterial-sulfate CNCs[56] was much shorter (567 nm ± 296 nm) than the average length measured here (1103 nm ± 698 nm), leading to a much lower average aspect ratio ($L/h \approx 31 \pm 16$) than the average aspect ratio ($L/h \approx 94 \pm 79$) reported here (Figure 6). By contrast, the tunicate CNCs did not tend to bundle, giving less polydisperse height measurements compared to the bacterial-sulfate CNCs. The average length (1073 nm ± 719 nm) and average thickness (9.2 nm ± 2.1 nm) reported in the literature for tunicate-sulfate CNCs[57,58] are comparable to the average length (1187 nm ± 1066 nm) and thickness (9.4 nm ± 5.0 nm) measured here (Figure 6). The wood-sulfate CNCs had the lowest aspect ratio and the narrowest size distribution of the nanocelluloses measured in this study. Average length (141 nm ± 6 nm) and height (5.0 nm ± 0.3 nm) reported in the literature for wood-sulfate CNCs[59] were very similar to the length (130 nm ± 67 nm) and height (5.9 nm ± 1.8 nm) measured here (Figure 6). It is understandable that there would be some variation in fiber size and aspect ratio for CNCs. The heterogeneity, in size and aspect ratio, observed for these CNCs demonstrates the diffusion controlled nature of acid hydrolysis.[10]

Surface Energy. Information about the surface energy of nanocellulose is important for determining the effect of newly added surface functional groups and for determining the compatibility of the nanocellulose with various polymer matrixes to ensure optimal fiber–matrix interaction. Inverse gas chromatography (IGC) was used to measure the surface energy of the CNCs and CNFs. For these measurements, the various nanocellulose samples were placed in a chromatographic column as the stationary phase, and solvent probe molecules were injected into the carrier gas stream. The retention time and shape of the chromatogram gives information on surface heterogeneity, surface area, acid–base properties, and surface energy.[42] Traditional IGC experiments at infinite dilution are typically biased by high energy sites,[60,61] which may not be able to fully describe the surface properties. In this study, surface energy experiments were performed over a range of concentrations to more fully describe the energetic situation on the surfaces of the CNCs and CNFs.

Dispersive and acid–base surface energy profiles for each sample were measured and graphed in Figure 7. The surface energy is noticeably higher at low surface coverage for some of the samples, which can be due to surface defects or impurities (Figure 7). The bacterial CNC samples have a higher dispersive surface energy value (>53 mJ/m^2) than the tunicate or wood CNC samples (33–50 mJ/m^2) at 10% surface coverage (Figure 7a), these findings are comparable to literature values.[62,63] The acid–base surface energy profiles, based on the Good–van Oss–Chaudhury approach,[44,45] also show that the bacterial and tunicate nanocellulose samples have higher acid–base surface energy than the wood nanocellulose samples (Figure 7b). Papirer et al.[61] were able to demonstrate that nanocelluloses with high crystallinities also have higher surface energy values. This trend can also be seen in Figure 7. The more crystalline CNCs (bacterial and tunicate) have higher dispersive and acid–base values, in comparison to the more amorphous wood CNCs, which have lower dispersive and acid–base values. Higher surface energy values seen for bacterial CNCs can indicate that the surface is composed of more active surface groups or a higher density of surface groups.

Also, note that the range of dispersive surface energies is much larger (35–70 mJ/m^2) than the observed range of acid–base surface energies (4–12 mJ/m^2) (Figure 7a vs 7b). This suggests that the dispersive energy (hydrophobic) makes a much larger contribution to the total surface energy than does the acid–base surface energy (hydrophilic). This is consistent

with the "Lindman hypothesis," recently discussed in a review by several cellulose researchers,[64] which asserts that surface energy properties of cellulose should be viewed in the context of a hierarchy of different scales of interactions: from ionic interactions, to hydrogen bonding, and a larger contribution from hydrophobic interactions than had been included in the past.

Autofluorescent Impurities. To gain a better understanding of the nanocellulose's meso to micrometer scale morphology, we also imaged them using laser scanning confocal microscopy (LSCM). From reflection mode imaging (see Figure 8, top row), we observed particles that were tens to hundreds of micrometers in size in all of the samples. These are most likely hydrolysis-resistant particles. From confocal microscopy and NMR data, we concluded that these compounds makeup a small fraction of the total cellulose samples (detection limit of the NMR is 0.5 mol % for ^{13}C); however, their impact on the properties of the nanocellulose can be significant. As mentioned in the introduction, if the CNCs are used for biomedical applications, such non-nanocellulose impurities may cause biocompatibility problems.[65,66] If the CNCs are used in coatings and optical and composites applications, the impurities can be problematic. Furthermore, because the undigested particles are fluorescent (see Figure 8, bottom row), they can negatively affect fluorescence measurements and can make Raman imaging difficult.[67] However, the autofluorescence may also provide a powerful method for monitoring the completeness of purification during the CNC/CNF preparation process. Historically, fluorescence has been used in the pulp and paper industry for decades,[68] and can be employed as a quality assurance measurement during CNC/CNF manufacturing.

Identification of Autofluorescent Impurities. Knowing the general contents of the initial cellulose sources, it is believed that the fluorescent particles can be lignin (wood samples),[68] chlorophyll (wood samples),[69] or proteins (tunicate/bacterial samples). There are also reports of nonfluorescent compounds found in wood that turn into flavonoid fluorophores after soaking in alkaline water (*Lignum nephriticum*).[70] To gain additional information about the nature of the autofluorescent species in each of the nanocellulose samples, we employed Raman spectroscopy.

Raman spectroscopy of cellulose has been used by others to determine crystallinity;[67] here, it was used to gather chemical information on the autofluorescent particles in an attempt to identify (based on chemical functionality present) the composition or further distinguish (based on unique spectral features) these particles from cellulose. Raman spectroscopy is a useful measurement technique because it does not require a large sample volume and is generally, nondestructive.

Raman spectra of cellulose from three samples (bacterial-sulfate, tunicate sulfate, and wood-TEMPO) were collected (Figure 9a) and compared to the literature data.[71] Cellulose, being a polysaccharide, has characteristic Raman bands from 1000 to 1200 cm^{-1} corresponding to $\upsilon(C-O-C)$ asymmetric stretching and $\upsilon(C-C)$ stretches and Raman bands from 1300 to 1500 cm^{-1} corresponding to $\delta(CH_2)$ and $\delta(CH_2OH)$ deformations.[71] The three cellulose samples studied here have comparable Raman shifts with slight variation in the peak shapes likely resulting from light scattering, crystalline fraction, and cellulose phase/crystallinity effects.

Upon initial exposure to the excitation source, the autofluorescent particles' spectra exhibited a strong fluorescence background. This background initially obscures the Raman features, but after initial exposure, it is sufficiently reduced through photobleaching to allow for high fidelity Raman spectra to be recorded. The fluorescent, hydrolysis resistant particles in bacterial-HCl and bacterial-sulfate samples have nearly identical Raman spectra that are very distinctive from the Raman spectrum of cellulose (Figure 9b). Strong peaks at 696, 728, 1445, and 1640 cm^{-1} are unique to the fluorescent particles in both bacterial cellulose samples and can be associated with undigested proteins in the bacterial cell membrane as well as other naturally occurring fluorescent molecules found in bacteria. The peaks at 696 and 728 cm^{-1} can be assigned to $\upsilon(C-S)$ aliphatic stretching,[72] and the peak at 1640 cm^{-1} can be assigned to amide, $\upsilon(C=C)$, or $\upsilon(C=N)$ stretching, which are all functional groups present in proteins.[73]

The fluorescent micrometer-sized particles in tunicate-sulfate can also be associated with undigested proteins, as well as other naturally occurring fluorescent molecules. The fluorescent particles in the tunicate sample were not readily photobleached, and the resulting Raman spectrum was dominated by the fluorescence background (Figure 9c). Although the presence of the background limits analysis of these particles, a Raman peak at 1607 cm^{-1} is resolvable and is distinctive from the cellulose Raman spectrum. The peak is potentially due to aromatic $\upsilon(CC)$ stretches given its location and given that aromatic compounds typically exhibit strong fluorescence.[74]

The wood cellulose samples had the lowest fluorescence intensity and the autofluorescence generally corresponded to only large, unhydrolyzed wood fibers. These large fibers contained cellulose along with lignin and other fluorescent molecules, thus the Raman spectra for the autofluorescent particles in the wood samples were dominated by cellulose peaks (Figure 9d). The cellulose bands can be removed by normalizing the two Raman spectra and subtracting the wood cellulose spectrum from the autofluorescent particle spectrum. This highlights the difference between the two spectra. Peaks at 859, 1448, and 1747 cm^{-1} are unique to the fluorescent, hydrolysis resistant particles in the wood-TEMPO sample. The peak at 859 cm^{-1} can be assigned to $\upsilon(C-O-C)$ stretching and the peak at 1747 cm^{-1} can be assigned to $\upsilon(C=C)$ and $\upsilon(C=O)$ stretching, all of which are chemical functionalities present in lignin.[75] The Raman data provides clear evidence for the presence of chemical compounds other than cellulose in the samples. Both fluorescence microscopy and Raman spectroscopy prove to be potentially useful tools for monitoring the completeness of the nanocellulose preparation process.

CONCLUSIONS

A wide variety of measurement methods (AFM, TEM, ^{13}C–CPMAS-NMR spectroscopy, IGC, and Raman and fluorescent microscopy) were used to gather and compare structural and chemical information on seven CNCs and CNFs derived from natural sources (bacteria, tunicate, and wood) using typical hydrolysis conditions (acid, enzymatic, mechanical, and TEMPO-mediated oxidation). The information gathered here provides a direct comparison of many of the key properties (crystalline fraction, polymorph, structural morphology, aspect ratio, purity, and surface energy) of these new and important nanomaterials (see Table S2 in the Supporting Information for a data summary).

Our findings permit several general conclusions associated with this diverse set of materials. CNCs that are rodlike in appearance have a higher crystalline fraction than CNFs which

are fibrillar in appearance. Sizes and aspect ratios of the CNCs measured are dependent upon the source of the cellulose. The high crystalline fraction of the tunicate-sulfate CNCs lead to longer rodlike particles and higher aspect ratio, whereas the lower crystalline fraction of the wood-sulfate CNCs yielded shorter rodlike particles and lower aspect ratio. IGC surface energy measurements revealed that hydrophobic interactions make a major contribution to the total surface energy of both types of cellulose. In all cases, a trace amount of naturally occurring fluorescent compounds were observed after hydrolysis. Confocal microscopy was used to locate these autofluorescent impurities, with morphology and optical (fluorescent) properties substantially different from the nanocellulose. Raman microscopy was used to confirm that the fluorescent species were unique for each cellulose source. The fluorescence and Raman microscopy data also demonstrated that such methods may be useful for monitoring purity during CNC/CNF processing. This study demonstrates that by varying the hydrolysis techniques, and/or the source of the cellulose, important properties and characteristics of nanocellulose can be tuned.

■ ASSOCIATED CONTENT

Supporting Information

More information on how the aspect ratio measurements were done, as well as additional AFM images and characterization tables. This material is available free of charge via the Internet at http://pubs.acs.org.

■ AUTHOR INFORMATION

Corresponding Author

*E-mail: jeffrey.gilman@nist.gov. Tel.: 301-975-6573.

Author Contributions

The manuscript was written through contributions of all authors. All authors have given approval to the final version of the manuscript.

Funding

AFOSR (MIPR F1ATA03239G001 A1). Swiss National Science Foundation (NRP 62: Smart Materials, Nr. 406240_126046). Lars-Erik Thunholms Foundation for promotion of scientific research.

Notes

The authors declare no competing financial interest.

■ ACKNOWLEDGMENTS

We thank Christopher Stafford at NIST for his help in AFM data collection and image analysis. We also thank Douglas Fox at American University for providing us with nanocellulose samples.

■ REFERENCES

(1) Mukherjee, S. M.; Woods, H. J. X-ray and Electron Miroscope Sudies of the Degradation of Cellulose by Sulfuric Acid. *Biochim. Biophys. Acta* **1953**, *10* (4), 499−511.

(2) Wang, B.; Sain, M.; Oksman, K. Study of Structural Morphology of Hemp Fiber from the Micro to the Nanoscale. *Appl. Compos. Mater.* **2007**, *14* (2), 89−103.

(3) Saddler, J. N.; Brownell, H. H.; Clermont, L. P.; Levitin, N. Enzymatic-Hydrolysis of Cellulose and Various Pretreated Wood Fractions. *Biotechnol. Bioeng.* **1982**, *24* (6), 1389−1402.

(4) Lima, A. M. D.; Wong, J. T.; Paillet, M.; Borsali, R.; Pecora, R. Translational and Rotational Dynamics of Rodlike Cellulose Whiskers. *Langmuir* **2003**, *19* (1), 24−29.

(5) Lima, M. M. D.; Borsali, R. Static and Dynamic Light Scattering from Polyelectrolyte Microcrystal Cellulose. *Langmuir* **2002**, *18* (4), 992−996.

(6) Beltrame, P. L.; Paglia, E. D.; Seves, A.; Pellizzoni, E.; Romano, M. Structural Features of Native Cellulose Gels and Films from Their Susceptibility to Enzymatic Attack. *J. Appl. Polym. Sci.* **1992**, *44* (12), 2095−2101.

(7) Hohl, H. R.; Jehli, J. Presence of Cellulose Microfibrils in Proteinaceous Slime Track of Dictyostelium-Discoideum. *Arch. Mikrobiol.* **1973**, *92* (3), 179−187.

(8) Reiner, R. S.; Rudie, A. W. Process Scale-Up of Cellulose Nanocrystal Production to 25 kg Batch at the Forest Products Laboratory. In *Production and Application of Cellulose Nanomaterials*; Postek, M. T., Moon, R. J., Rudie, A. W., Bilodeau, M. A., Eds.; TAPPI Press: Peachtree Corners, GA, 2013; pp 21−24.

(9) Reiner, R. S.; Rudie, A. W. Pilot Plant Scale-Up of TEMPO-Pretreated Cellulose Nanofibrils. In *Production and Application of Cellulose Nanomaterials*; Postek, M. T., Moon, R. J., Rudie, A. W., Bilodeau, M. A., Eds.; TAPPI Press: Peachtree Corners, GA, 2013; pp 177−178.

(10) Habibi, Y.; Lucia, L. A.; Rojas, O. J. Cellulose Nanocrystals: Chemistry, Self-Assembly, and Applications. *Chem. Rev.* **2010**, *110* (6), 3479−3500.

(11) Dong, X. M.; Revol, J. F.; Gray, D. G. Effect of Microcrystallite Preparation Conditions on the Formation of Colloid Crystals of Cellulose. *Cellulose* **1998**, *5* (1), 19−32.

(12) Saito, T.; Isogai, A. TEMPO-Mediated Oxidation of Native Cellulose. The Effect of Oxidation Conditions on Chemical and Crystal Structures of the Water-Insoluble Fractions. *Biomacromolecules* **2004**, *5* (5), 1983−1989.

(13) Hasani, M.; Cranston, E. D.; Westman, G.; Gray, D. G. Cationic Surface Functionalization of Cellulose Nanocrystals. *Soft Matter* **2008**, *4* (11), 2238−2244.

(14) Roy, D.; Semsarilar, M.; Guthrie, J. T.; Perrier, S. Cellulose Modification by Polymer Grafting: A Review. *Chem. Soc. Rev.* **2009**, *38* (7), 2046−2064.

(15) Favier, V.; Chanzy, H.; Cavaille, J. Y. Polymer Nanocomposites Reinforced by Cellulose Whiskers. *Macromolecules* **1995**, *28* (18), 6365−6367.

(16) Moon, R. J.; Martini, A.; Nairn, J.; Simonsen, J.; Youngblood, J. Cellulose Nanomaterials Review: Structure, Properties and Nanocomposites. *Chem. Soc. Rev.* **2011**, *40* (7), 3941−3994.

(17) Clift, M. J. D.; Foster, E. J.; Vanhecke, D.; Studer, D.; Wick, P.; Gehr, P.; Rothen-Rutishauser, B.; Weder, C. Investigating the Interaction of Cellulose Nanofibers Derived from Cotton with a Sophisticated 3D Human Lung Cell Coculture. *Biomacromolecules* **2011**, *12* (10), 3666−3673.

(18) Eichhorn, S. J.; Dufresne, A.; Aranguren, M.; Marcovich, N. E.; Capadona, J. R.; Rowan, S. J.; Weder, C.; Thielemans, W.; Roman, M.; Renneckar, S.; Gindl, W.; Veigel, S.; Keckes, J.; Yano, H.; Abe, K.; Nogi, M.; Nakagaito, A. N.; Mangalam, A.; Simonsen, J.; Benight, A. S.; Bismarck, A.; Berglund, L. A.; Peijs, T. Review: Current International Research into Cellulose Nanofibres and Nanocomposites. *J. Mater. Sci.* **2010**, *45* (1), 1−33.

(19) Kelly, J. A.; Shukaliak, A. M.; Cheung, C. C. Y.; Shopsowitz, K. E.; Hamad, W. Y.; MacLachlan, M. J. Responsive Photonic Hydrogels Based on Nanocrystalline Cellulose. *Angew. Chem., Int. Ed.* **2013**, *52* (34), 8912−8916.

(20) Fukuzumi, H.; Saito, T.; Wata, T.; Kumamoto, Y.; Isogai, A. Transparent and High Gas Barrier Films of Cellulose Nanofibers Prepared by TEMPO-Mediated Oxidation. *Biomacromolecules* **2009**, *10* (1), 162−165.

(21) Mendez, J.; Annamalai, P. K.; Eichhorn, S. J.; Rusli, R.; Rowan, S. J.; Foster, E. J.; Weder, C. Bioinspired Mechanically Adaptive Polymer Nanocomposites with Water-Activated Shape-Memory Effect. *Macromolecules* **2011**, *44* (17), 6827−6835.

(22) Biyani, M. V.; Foster, E. J.; Weder, C. Light-Healable Supramolecular Nanocomposites Based on Modified Cellulose Nanocrystals. *ACS Macro Lett.* **2013**, *2* (3), 236−240.

(23) Potter, K. A.; Jorfi, M.; Householder, K. T.; Foster, E. J.; Weder, C.; Capadona, J. R. Curcumin-Releasing Mechanically Adaptive Intracortical Implants Improve the Proximal Neuronal Density and Blood−Brain Barrier Stability. *Acta Biomaterialia* **2014**, *10* (5), 2209−2222.
(24) Capadona, J. R.; Shanmuganathan, K.; Tyler, D. J.; Rowan, S. J.; Weder, C. Stimuli-Responsive Polymer Nanocomposites Inspired by the Sea Cucumber Dermis. *Science* **2008**, *319* (5868), 1370−1374.
(25) Shanmuganathan, K.; Capadona, J. R.; Rowan, S. J.; Weder, C. Biomimetic Mechanically Adaptive Nanocomposites. *Prog. Polym. Sci.* **2010**, *35* (1−2), 212−222.
(26) Hsu, L.; Weder, C.; Rowan, S. J. Stimuli-Responsive, Mechanically-Adaptive Polymer Nanocomposites. *J. Mater. Chem* **2011**, *21* (9), 2812−2822.
(27) Ma, H. Y.; Hsiao, B. S.; Chu, B. Ultrafine Cellulose Nanofibers as Efficient Adsorbents for Removal of UO22+ in Water. *ACS Macro Lett.* **2012**, *1* (1), 213−216.
(28) Capadona, J. R.; Tyler, D. J.; Zorman, C. A.; Rowan, S. J.; Weder, C. Mechanically Adaptive Nanocomposites for Neural Interfacing. *MRS Bull.* **2012**, *37* (6), 581−589.
(29) Eichhorn, S. J. Cellulose Nanowhiskers: Promising Materials for Advanced Applications. *Soft Matter* **2011**, *7* (2), 303−315.
(30) Sakurada, I.; Nukushina, Y.; Ito, T. Experimental Determination of Elastic Modulus of Crystalline Regions in Oriented Polymers. *J. Polym. Sci.* **1962**, *57* (165), 651−660.
(31) Dufresne, A. Polysaccharide Nano Crystal Reinforced Nanocomposites. *Can. J. Chem.* **2008**, *86* (6), 484−494.
(32) Eichhorn, S. J. Stiff as a Board: Perspectives on the Crystalline Modulus of Cellulose. *ACS Macro Lett.* **2012**, *1* (11), 1237−1239.
(33) Fox, D. M.; Lee, J.; Zammarano, M.; Katsoulis, D.; Eldred, D. V.; Haverhals, L. M.; Trulove, P. C.; De Long, H. C.; Gilman, J. W. Char-Forming Behavior of Nanofibrillated Cellulose Treated with Glycidyl Phenyl POSS. *Carbohydr. Polym.* **2012**, *88* (3), 847−858.
(34) *Production and Application of Cellulose Nanomaterials*; Postek, M. T., Moon, R. J., Rudie, A. W., Bilodeau, M. A., Eds.; TAPPI Press: Peachtree Corners, GA, 2013.
(35) Zammarano, M.; Maupin, P. H.; Sung, L. P.; Gilman, J. W.; McCarthy, E. D.; Kim, Y. S.; Fox, D. M. Revealing the Interface in Polymer Nanocomposites. *ACS Nano* **2011**, *5* (4), 3391−3399.
(36) Postek, M. T.; Vladar, A.; Dagata, J.; Farkas, N.; Ming, B.; Wagner, R.; Raman, A.; Moon, R. J.; Sabo, R.; Wegner, T. H.; Beecher, J., Development of the Metrology and Imaging of Cellulose Nanocrystals. *Meas. Sci. Technol.* **2011**, *22* (2).
(37) Ciesielski, P. N.; Matthews, J. F.; Tucker, M. P.; Beckham, G. T.; Crowley, M. F.; Himmel, M. E.; Donohoe, B. S. 3D Electron Tomography of Pretreated Biomass Informs Atomic Modeling of Cellulose Microfibrils. *ACS Nano* **2013**, *7* (9), 8011−8019.
(38) Olsson, R. T.; Kraemer, R.; Lopez-Rubio, A.; Torres-Giner, S.; Ocio, M. J.; Lagaron, J. M. Extraction of Microfibrils from Bacterial Cellulose Networks for Electrospinning of Anisotropic Biohybrid Fiber Yarns. *Macromolecules* **2010**, *43* (9), 4201−4209.
(39) Favier, V.; Chanzy, H.; Cavaille, J. Y. Polymer Nanocomposites Reinforced by Cellulose Whiskers. *Macromolecules* **1995**, *28*, 6365−6367.
(40) Jorfi, M.; Roberts, M. N.; Foster, E. J.; Weder, C. Physiologically Responsive, Mechanically Adaptive Bio-Nanocomposites for Biomedical Applications. *ACS Appl. Mater. Interfaces* **2013**, *5* (4), 1517−1526.
(41) Burnett, D. J.; Khoo, J.; Naderi, M.; Heng, J. Y. Y.; Wang, G. D.; Thielmann, F. Effect of Processing Route on the Surface Properties of Amorphous Indomethacin Measured by Inverse Gas Chromatography. *AAPS PharmSciTech* **2012**, *13* (4), 1511−1517.
(42) Dorris, G. M.; Gray, D. G. Adsorption of Normal-Alkanes at Zero Surface Coverage on Cellulose Paper and Wood Fibers. *J. Colloid Interface Sci.* **1980**, *77* (2), 353−362.
(43) Donnet, J. B.; Park, S. J.; Balard, H. Evaluation of Specific Interactions of Solid-Surfaces by Inverse Gas-Chromatography - a New Approach Based on Polarizability of the Probes. *Chromatographia* **1991**, *31* (9−10), 434−440.
(44) Good, R. J. *Contact Angle, Wettability and Adhesion*; VSP: Utrecht, The Netherlands, 2003; Vol. 3.
(45) van Oss, C. J. *Interfacial Forces in Aqueous Media*; Marcel Dekker: New York, 1994.
(46) Vaudin, M. D.; Gerbig, Y. B.; Stranick, S. J.; Cook, R. F., Comparison of Nanoscale Measurements of Strain and Stress Using Electron Back Scattered Diffraction and Confocal Raman Microscopy. *Appl. Phys. Lett.* **2008**, *93* (19).
(47) van den Berg, O.; Capadona, J. R.; Weder, C. Preparation of Homogeneous Dispersions of Tunicate Cellulose Whiskers in Organic Solvents. *Biomacromolecules* **2007**, *8* (4), 1353−1357.
(48) Briois, B.; Saito, T.; Petrier, C.; Putaux, J. L.; Nishiyama, Y.; Heux, L.; Molina-Boisseau, S. I-Alpha -> I-Beta Transition of Cellulose under Ultrasonic Radiation. *Cellulose* **2013**, *20* (2), 597−603.
(49) Andersson, S.; Wikberg, H.; Pesonen, E.; Maunu, S. L.; Serimaa, R. Studies of Crystallinity of Scots Pine and Norway Spruce Cellulose. *Trees−Struct. Funct.* **2004**, *18* (3), 346−353.
(50) Atalla, R. H.; Vanderhart, D. L. Native Cellulose−A Composite of 2 Distinct Crystalline Forms. *Science* **1984**, *223* (4633), 283−285.
(51) Atalla, R. H.; VanderHart, D. L. The Role of Solid State C-13 NMR Spectroscopy in Studies of the Nature of Native Celluloses. *Solid State Nucl. Magn. Reson.* **1999**, *15* (1), 1−19.
(52) Colvin, J. R. The Mechanism of Formation of Cellulose-Like Microfibrils in a Cell-Free System from Acetobacter-Xylinum. *Planta* **1980**, *149* (2), 97−107.
(53) Paakko, M.; Ankerfors, M.; Kosonen, H.; Nykanen, A.; Ahola, S.; Osterberg, M.; Ruokolainen, J.; Laine, J.; Larsson, P. T.; Ikkala, O.; Lindstrom, T. Enzymatic Hydrolysis Combined with Mechanical Shearing and High-Pressure Homogenization for Nanoscale Cellulose Fibrils and Strong Gels. *Biomacromolecules* **2007**, *8* (6), 1934−1941.
(54) Hanley, S. J.; Giasson, J.; Revol, J. F.; Gray, D. G. Atomic Force Microscopy of Cellulose Microfibrils - Comparison with Transmission Electron-Microscopy. *Polymer* **1992**, *33* (21), 4639−4642.
(55) Bengio, E. A.; Tsentalovich, D. E.; Behabtu, N.; Kleinerman, O.; Kesselman, E.; Schmidt, J.; Talmon, Y.; Pasquali, M. Statistical Length Measurement Method by Direct Imaging of Carbon Nanotubes. *ACS Appl. Mater. Interfaces* **2014**, Submitted.
(56) Martinez-Sanz, M.; Lopez-Rubio, A.; Lagaron, J. M. Optimization of the Nanofabrication by Acid Hydrolysis of Bacterial Cellulose Nanowhiskers. *Carbohydr. Polym.* **2011**, *85* (1), 228−236.
(57) Elazzouzi-Hafraoui, S.; Nishiyama, Y.; Putaux, J. L.; Heux, L.; Dubreuil, F.; Rochas, C. The Shape and Size Distribution of Crystalline Nanoparticles Prepared by Acid Hydrolysis of Native Cellulose. *Biomacromolecules* **2008**, *9* (1), 57−65.
(58) Bercea, M.; Navard, P. Shear Dynamics of Aqueous Suspensions of Cellulose Whiskeys. *Macromolecules* **2000**, *33* (16), 6011−6016.
(59) Beck-Candanedo, S.; Roman, M.; Gray, D. G. Effect of Reaction Conditions on the Properties and Behavior of Wood Cellulose Nanocrystal Suspensions. *Biomacromolecules* **2005**, *6* (2), 1048−1054.
(60) Felix, J. M.; Gatenholm, P.; Schreiber, H. P. Controlled Interactions in Cellulose-Polymer Composites 0.1. Effect on Mechanical-Properties. *Polym. Compos.* **1993**, *14* (6), 449−457.
(61) Papirer, E.; Brendle, E.; Balard, H.; Vergelati, C. Inverse Gas Chromatography Investigation of the Surface Properties of Cellulose. *J. Adhes. Sci. Technol.* **2000**, *14* (3), 321−337.
(62) Pommet, M.; Juntaro, J.; Heng, J. Y. Y.; Mantalaris, A.; Lee, A. F.; Wilson, K.; Kalinka, G.; Shaffer, M. S. P.; Bismarck, A. Surface Modification of Natural Fibers Using Bacteria: Depositing Bacterial Cellulose onto Natural Fibers to Create Hierarchical Fiber Reinforced Nanocomposites. *Biomacromolecules* **2008**, *9* (6), 1643−1651.
(63) Heng, J. Y. Y.; Pearse, D. F.; Thielmann, F.; Lampke, T.; Bismarck, A. Methods to Determine Surface Energies of Natural Fibres: A Review. *Compos. Interfaces* **2007**, *14* (7−9), 581−604.
(64) Glasser, W. G.; Atalla, R. H.; Blackwell, J.; Brown, R. M.; Burchard, W.; French, A. D.; Klemm, D. O.; Nishiyama, Y. About the Structure of Cellulose: Debating the Lindman Hypothesis. *Cellulose* **2012**, *19* (3), 589−598.
(65) Huby, R. D. J.; Dearman, R. J.; Kimber, I. Why are Some Proteins Allergens? *Toxicol. Sci.* **2000**, *55* (2), 235−246.

(66) Wagner, S.; Breiteneder, H. The Latex-Fruit Syndrome. *Biochem. Soc. Trans.* **2002**, *30*, 935−940.
(67) Agarwal, U. P.; Reiner, R. R.; Ralph, S. A. Estimation of Cellulose Crystallinity of Lignocelluloses Using Near-IR FT-Raman Spectroscopy and Comparison of the Raman and Segal-WAXS Methods. *J. Agric. Food. Chem.* **2013**, *61* (1), 103−113.
(68) Olmstead, J. A.; Gray, D. G. Fluorescence Spectroscopy of Cellulose, Lignin and Mechanical Pulps: A Review. *J. Pulp Pap. Sci.* **1997**, *23* (12), J571−J581.
(69) Taylor, J. G.; Haigler, C. H.; Kilburn, D. G.; Blanton, R. L. Detection of Cellulose with Improved Specificity Using Laser-Based Instruments. *Biotech. Histochem.* **1996**, *71* (5), 215−223.
(70) Ulises Acuna, A.; Amat-Guerri, F.; Morcillo, P.; Liras, M.; Rodriguez, B. Structure and Formation of the Fluorescent Compound of Lignum Nephriticum. *Org. Lett.* **2009**, *11* (14), 3020−3023.
(71) De Gelder, J.; De Gussem, K.; Vandenabeele, P.; Moens, L. Reference Database of Raman Spectra of Biological Molecules. *J. Raman Spectrosc.* **2007**, *38* (9), 1133−1147.
(72) Edsall, J. T.; Otvos, J. W.; Rich, A. Raman Spectra of Amino Acids and Related Compounds 0.7. Glycylglycine, Cysteine, Cystine and Other Amino Acids. *J. Am. Chem. Soc.* **1950**, *72* (1), 474−477.
(73) Maiti, N. C.; Apetri, M. M.; Zagorski, M. G.; Carey, P. R.; Anderson, V. E. Raman Spectroscopic Characterization of Secondary Structure in Natively Unfolded Proteins: Alpha-Synuclein. *J. Am. Chem. Soc.* **2004**, *126* (8), 2399−2408.
(74) Larkin, P. J. *Infrared and Raman Spectroscopy; Principles and Spectral Interpretation*; Elsevier: Waltham, MA, 2011.
(75) Agarwal, U. P.; Ralph, S. A. FT-Raman Spectroscopy of Wood: Identifying Contributions of Lignin and Carbohydrate Polymers in the Spectrum of Black Spruce (*Picea mariana*). *Appl. Spectrosc.* **1997**, *51* (11), 1648−1655.